

Gravity wave generation by convection and momentum deposition in the mesosphere-lower thermosphere

R. A. Vincent,¹ M. J. Alexander,² B. K. Dolman,^{1,3} A. D. MacKinnon,¹ P. T. May,^{1,4} S. Kovalam,¹ and I. M. Reid¹

Received 18 November 2012; revised 7 March 2013; accepted 25 March 2013; published 25 June 2013.

[1] The Tropical Warm Pool International Cloud Experiment campaign centered on Darwin (12°S, 131°E) in northern Australia in January–February 2006 provided an opportunity to study gravity wave generation by convection and the associated wave propagation and momentum transport. In this study, we discuss wave generation by a single mesoscale convective system (MCS) that occurred on 23 January. The project used a variety of radars to study the spatial and temporal variability of rainfall and the associated latent heat release during the storm. A high-resolution numerical model utilized the latent heat release derived from radar rainfall measurements to compute the spatial and geographic variation of gravity wave generation and propagation into the lower stratosphere. Gravity wave ray-tracing techniques were then used to estimate the wave energy flux penetrating to heights near 90 km, where the results were compared with direct measurements made with a meteor wind radar. This comparison is used to calibrate the momentum fluxes derived from the model and the ray-tracing results using an iterative technique. The momentum was deposited in a relatively compact region. Body forces computed from the flux divergences had their maximum values at heights near 98 km with a peak values of about $400 \text{ m s}^{-1} \text{ h}^{-1}$. The effects of secondary gravity wave generation are discussed, as is the overall contribution of gravity waves generated by MCSs to the momentum budget of the tropical middle atmosphere.

Citation: Vincent, R. A., M. J. Alexander, B. K. Dolman, A. D. MacKinnon, P. T. May, S. Kovalam, and I. M. Reid (2013), Gravity wave generation by convection and momentum deposition in the mesosphere-lower thermosphere, *J. Geophys. Res. Atmos.*, 118, 6233–6245, doi:10.1002/jgrd.50372.

1. Introduction

[2] It is well known that gravity waves play an important role in determining the state and mean circulation of the middle and upper atmosphere [see the review by *Fritts and Alexander*, 2003]. However, despite many studies using a variety of ground-based, in situ and satellite techniques, there is still a significant lack of understanding of the relative importance of various gravity wave (GW) sources in determining the momentum budget of the middle atmosphere. Wave forcing by air flowing over topography is probably the best understood wave source and mountain wave drag parameterization schemes are incorporated routinely in weather prediction and climate models

[e.g., *Palmer et al.*, 1986]. A variety of parameterization schemes have been proposed to include the effects of non-orographic sources such as convective storms, wind shears, and geostrophic adjustment. These schemes may incorporate discrete waves or use spectral representations of the wave parameters [e.g., *Lindzen*, 1981; *Hines*, 1997; *Alexander and Dunkerton*, 1999; *Warner and McIntyre*, 2001]. Recently, GW parameterizations designed specifically for convective sources [e.g., *Beres et al.*, 2005; *Song et al.*, 2007] have been included in models. The common problem, however, is that observations do not adequately constrain the schemes. Better parameterization schemes can result only from a better understanding of the physical mechanisms by which waves are forced by different sources and the key characteristics (wavelengths, phase speeds, momentum fluxes) of the waves that are generated.

[3] Another issue in parameterization schemes is that of wave intermittency. Gravity wave forcing is not steady. Rather, wave sources are intermittent in space and time and so wave driving of the mean circulation is due to the superposition of many wave effects from many wave sources.

[4] Cumulus convection is an important wave source, particularly in the tropics. Recent modeling studies include *Piani et al.* [2000], *Song et al.* [2003], *Beres et al.* [2004],

¹School of Chemistry and Physics, The University of Adelaide, Adelaide, South Australia, Australia.

²NorthWest Research Associates, Inc., Boulder, Colorado, USA.

³ATRAD, Adelaide, South Australia, Australia.

⁴Centre for Australian Weather and Climate Research (CAWCR), Melbourne, Victoria, Australia.

Corresponding author: R. A. Vincent, School of Chemistry and Physics, The University of Adelaide, Adelaide, SA 5005, Australia. (robert.vincent@adelaide.edu.au)

Lane and Moncrieff [2008], and *Grimsdell et al.* [2010]. At least three linearized mechanisms for wave generation within storms have been proposed: The “mechanical oscillator” and “moving mountain” mechanisms describe forcing terms for the linearized momentum equation, and “transient latent heating” describes the forcing term for the thermodynamic equation. In reality, these three mechanisms will be coupled via nonlinear effects. *Song et al.* [2003] showed in a model study of convection that the heating term alone accurately described the wave spectrum, although the wave amplitudes were overestimated because the momentum forcing terms partly canceled the thermal forcing amplitude. They did not, however, significantly alter its shape or time variations. The wave spectrum generated by convection is known to be very sensitive to these details of the thermal forcing [*Alexander and Holton*, 2004; *Beres et al.*, 2004; *Kim et al.*, 2007]. The influence of convectively generated gravity waves is felt throughout the middle atmosphere and up into the thermosphere-ionosphere. Studies such as those of *Holton and Alexander* [1999], *Horinouchi et al.* [2002], *Vadas et al.* [2003], *Horinouchi* [2004], and *Vadas and Liu* [2009] demonstrated wave breakdown, mean-flow forcing, secondary wave emission, and wave effects on airglow emissions. There is an increasing focus on secondary wave generation by breaking gravity waves as the secondary waves can transfer momentum back down to the lower as well as higher into the upper atmosphere [*Vadas et al.*, 2003; *Lane and Sharman*, 2006; *Chun and Kim*, 2008; *Vadas and Liu*, 2009; *Vadas and Crowley*, 2010].

[5] Advances in understanding of wave generation by convection have been stimulated in part by observational campaigns conducted during the past two decades. Tropical Ocean Global Atmosphere Coupled Ocean Atmosphere Response Experiment concentrated on oceanic convection over the warm pool in the western Pacific [*Webster and Lukas*, 1992]. Maritime Continent Thunderstorm Experiment was organized around the intense island thunderstorms (Hectors) that occur on the Tiwi Islands near Darwin and their forcing and evolution, while the focus of the Darwin Area Wave Experiment (DAWEX) was also on similar storms and the generation of gravity waves and their propagation into the middle atmosphere [*Alexander et al.*, 2004; *Hamilton et al.*, 2004; *Vincent et al.*, 2004; *Hecht et al.*, 2004]. Nevertheless, there are few detailed observations against which high-resolution models can be compared [*Lane et al.*, 2003].

[6] Here we discuss a study of gravity waves that took place during the Tropical Warm Pool International Cloud Experiment (TWPICE) in January and February 2006. TWPICE was centered around Darwin (12.5°S, 130.5°E) in northern Australia and had the primary aim of describing tropical cloud systems and their environmental setting and impacts [*May et al.*, 2008]. The experiment took advantage of the large range of meteorological instrumentation in the vicinity of Darwin, including a polarimetric weather radar and a suite of cloud remote-sensing instruments. This was augmented by a dense network of radiosonde soundings, together with radiation, flux, lightning, remote-sensing measurements, and oceanographic and aircraft observations (see *May et al.* [2008] for further details).

[7] The wide range of observations made during TWPICE provided an excellent opportunity to study the generation

of GW by convective systems during the campaign, in which there were four distinct convective regimes. The period between 21 and 25 January was classified as a convectively active monsoon period, followed by a convectively suppressed monsoon period from 26 January to 3 February. After 3 days of clear skies, the intensive observation period concluded with a break period from 6 to 14 February.

[8] Here we focus on observations made on 23 January when a major mesoscale convective system passed through the Darwin area, leading to the largest daily rainfall during the TWPICE campaign. It gave us the opportunity to study gravity wave generation, propagation, and momentum flux deposition in the middle atmosphere due to a single convective event. In section 2, we summarize the instrumentation and the numerical model used in the study and briefly review the temporal and spatial variability of the rainfall in the Darwin area that is used to compute the latent heat release that seeds the model. The gravity wave spectrum computed by the model at the tropopause is described in section 3 and this is followed in section 4 by description of the gravity wave ray tracing and results. Section 5 discusses the spatial and temporal variability of the momentum fluxes derived from the ray-tracing study and momentum flux deposition, while the implications of our findings are discussed in section 6.

2. Instrumentation and Model

[9] The instruments used in this study were located at sites near Darwin. A vertically pointing 54 MHz boundary layer radar (BLR) was located at the Department of Environment's Atmospheric Radiation Measurement (ARM) Climate Research Facility (12.42°S, 130.88°E) at Darwin Airport. The BLR was essentially the same system that was situated on the Tiwi Islands during DAWEX [*Vincent et al.*, 2004]. Using three subgroups of antennas arranged in an equilateral triangle for reception and grouped together for transmission, the BLR measured winds in the lower troposphere using the spaced antenna technique. It was also possible to use the system in the Doppler mode to extract information on hydrometeor drops size distributions and precipitation rates as a function of height down to near ground level. In order to measure winds in the mesosphere-lower thermosphere (MLT), a meteor radar (MR) was placed at the Bureau of Meteorology's profiler site (12.42°S, 130.95°E). Winds measured by the meteor radar were derived using the methods described in *Holdsworth et al.* [2004]. For more details of the meteor radar and its capabilities, see *Vincent et al.* [2010].

[10] A key instrument in the TWPICE campaign and in our experiment was the C-band scanning polarimetric (CPol) radar located NE of Darwin at Gunn Point (12.25°S, 131.04°E). CPol undertakes a volume scan from near ground level up to heights near 20 km that provides three-dimensional hydrometeor distributions within a range of approximately 150 km of Gunn Point. Each scan takes about 10 min to complete. The horizontal coverage of the various instruments, together with the model domain (see below), is shown in Figure 1.

[11] On 23 January, there was almost continuous storm activity during this day with a burst of storm activity about

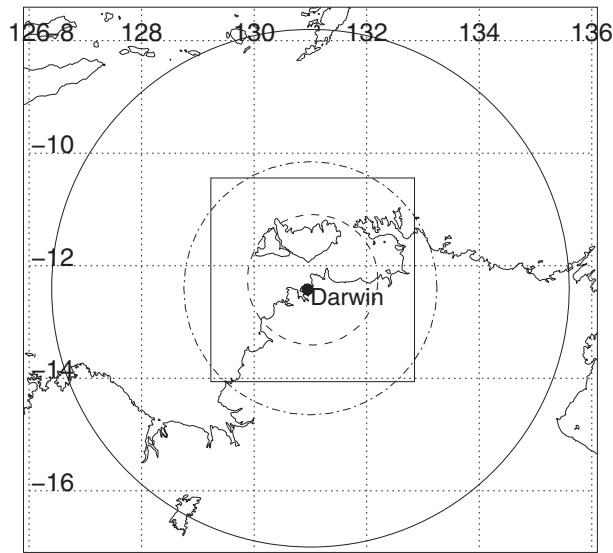


Figure 1. Map showing coverage of instruments and model in the vicinity of Darwin during TWICE. Meteor echoes were observed inside the region shown by the outer circle (solid), but the majority of meteors were observed at ranges shown by the inner circle (dash-dotted). The inner-most (dashed) circle shows the approximate coverage of the CPol radar, while the square shows the numerical model domain.

14 UTC producing an extensive high level cloud cover. This system also left a quasi-stationary set of cells aligned east west. At about 1630 UTC two small convective lines propagating from the NE and SE intersected the preexisting line at the same point and this initiated a significant cell with high rain rates south of the Tiwi islands. The convective area was a maximum at this time. As this complex developed cold pool outflows, a north-south oriented line was formed about 18 UTC with an extensive trailing stratiform

exhibiting deep cyclonic rotation. The deepest cells were at this time with 40 dBZ echoes reaching an altitude of 15 km and a spike in lightning activity suggesting very large vertical motions at this time. This line decreased in intensity and propagated outside the radar domain by about 22 UTC. It should be noted that this system subsequently had additional bursts of activity and generated a deep low to the southwest of Darwin.

[12] The left panel in Figure 2 shows a range-height intensity (RHI) profile taken by CPol over the profiler site on 23 January. The intense rain event centered on about 18 UTC with a duration of about 30 min is clearly evident. Another shorter duration (~ 10 min) and weaker, convective event was observed at about 19.5 UTC. The band of enhanced reflectivity seen over much of the day near an altitude of 4.5 km indicates the freezing level. The spatial variability of reflectivities measured by CPol at 18 UTC is illustrated in the right panel of Figure 2.

[13] The numerical model studies used here of gravity wave generation follow the methodology described in Alexander *et al.* [2004]. A high resolution nonlinear non-hydrostatic numerical model was used to simulate gravity wave generation by the convective storm. The model domain spanned $400 \text{ km} \times 400 \text{ km}$ in the horizontal and 25 km in the vertical, with horizontal and vertical resolutions of 2 km and 0.25 km, respectively.

[14] The model used the three-dimensional measurements of reflectivity from CPol to estimate realistic spatial and temporal patterns in rain rates within the approximately 150 km radius viewing area of the radar. The rain rates are derived from CPol reflectivities using the algorithms of Bringi *et al.* [2006, 2009]. They are then converted in turn to column convective heating rates. To force the model, the heating is distributed in a half-sine profile between 950 hPa and the cloud echo top height. The cloud-top height is determined as the highest altitude where radar reflectivity exceeds a typical noise level of 6 dBZ. Comparisons of waves forced with this model with Atmospheric

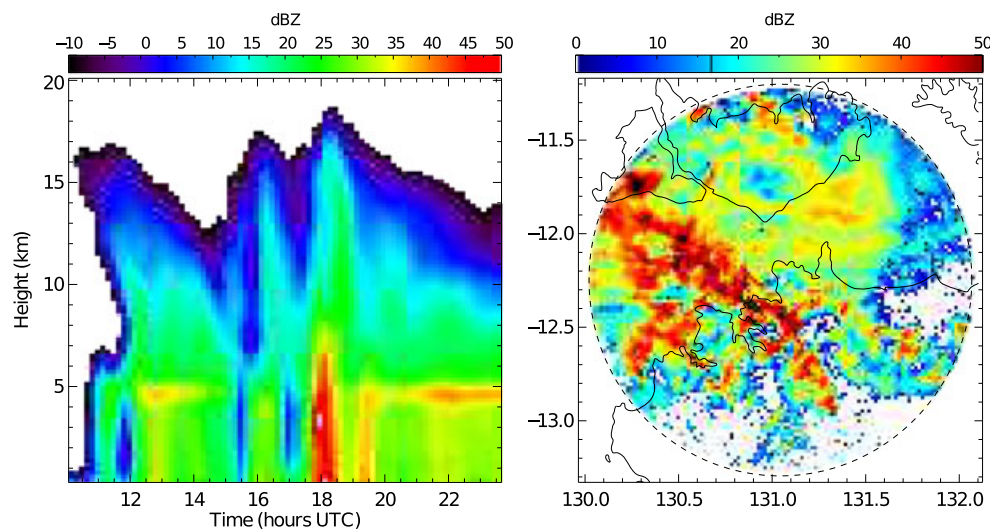


Figure 2. (left) Height-time intensity plot derived from vertical scans by the CPol radar over the profiler site on 23 January 2006. (right) CPol radar reflectivity map at a height of 1 km for 18 UTC.

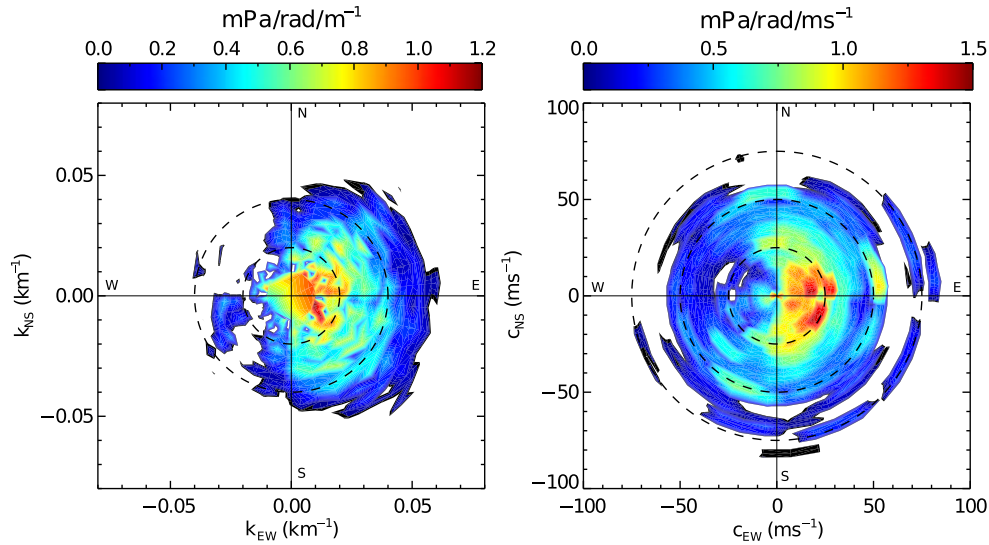


Figure 3. Angular spectra of gravity wave absolute momentum flux ($\rho_o[(\overline{u'w'})^2 + (\overline{v'w'})^2]^{1/2}$) derived from the mesoscale model at a height of 20 km for the 2 h interval centered on 18 UTC. (left) Spectra as a function of horizontal wave number. The inner and outer dashed circles indicate wavelengths of 50 and 25 km, respectively. (right) Momentum flux spectra as a function of horizontal ground-based phase speed. The dashed circles indicate phase speeds of 25, 50, and 75 m s^{-1} .

Infrared Sounder satellite shows good agreement in the phase structure of the waves in the stratosphere [Grimsdell *et al.*, 2010], which gives confidence in the wave amplitudes generated by the model.

3. Gravity Wave Source Spectra

[15] The mesoscale model described above was used to compute spectra of gravity wave momentum fluxes at the stratospheric levels of the model above 20 km. In order to capture the changes in the GW fluxes associated with the convective systems observed on 23 January 2006, it was decided to compute the fluxes in 2 h blocks, each overlapped by 1 h. In this way, the impact of gravity waves with periods of up to 120 min could be studied. Results were computed starting at 06 UTC and finishing at 22 UTC.

[16] Angular spectra of waves for the two-hour interval centered on 18 UTC are shown in Figure 3. The left-hand spectrum shows momentum flux plotted in terms of horizontal wave number while the right-hand spectrum is plotted in terms of horizontal ground-based phase speed. It is obvious that the waves are travelling predominately eastward as they enter the stratosphere.

[17] The dominant wavelengths and phase speeds are brought out more clearly in Figure 4, which shows energy content spectra as a function of phase speed and horizontal wave number, respectively. Energy content spectra ($x F(x)$) are convenient because $x F(x) d(\ln x)$ is the contribution to the total energy or variance [e.g., VanZandt, 1985]. Momentum fluxes peak for phase speeds in the range 10–50 m s^{-1} , with several discrete peaks evident, mainly at phase speeds between 15 and 30 m s^{-1} , and also one at just over 50 m s^{-1} . The wave number spectrum, however, is reasonably flat, with maximum fluxes in the range ~ 0.004 – 0.04 km^{-1} , equivalent to wavelengths in the range ~ 25 – 250 km .

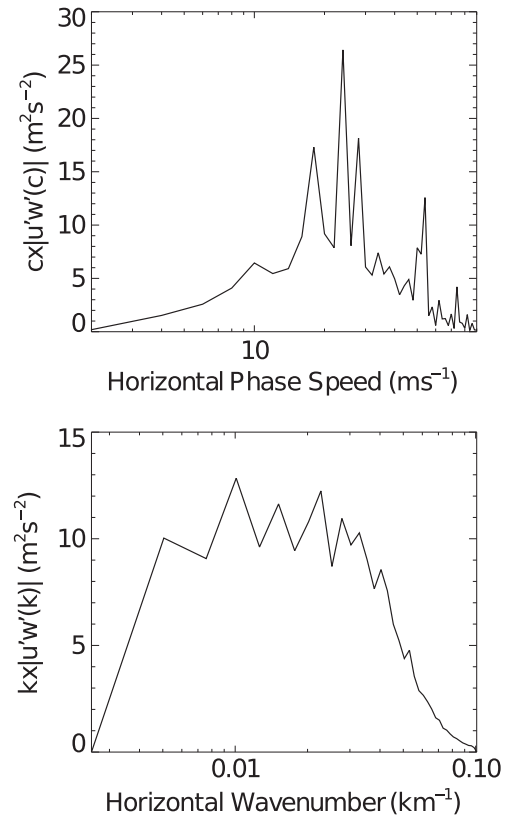


Figure 4. Absolute momentum flux at 18 UTC as a function of (top) ground-based phase speed and as a function of (bottom) horizontal wave number. The spectra are shown in area-preserving form.

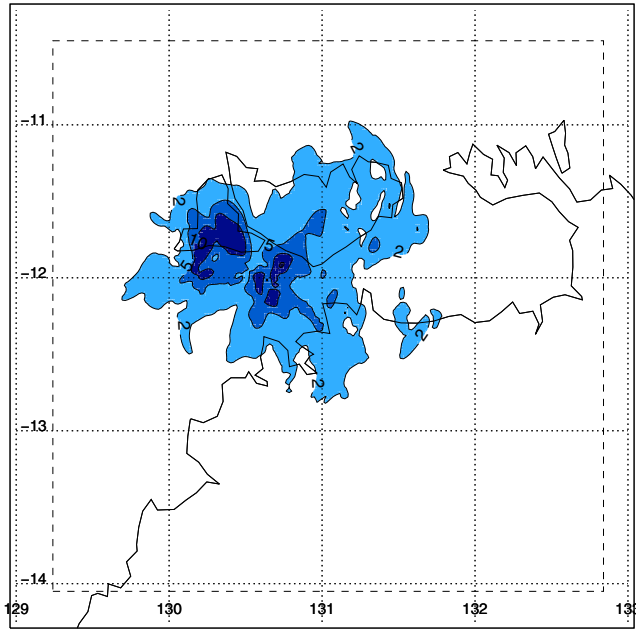


Figure 5. Geographic variation of momentum flux per unit mass ($\sqrt{|u'w'|^2 + |v'w'|^2}$) at 20 km altitude and 18 UTC as a function of latitude and longitude. The contour levels are 2, 5, 10, and 20 $\text{m}^2 \text{s}^{-2}$.

[18] Using the model output, gravity wave ray tracing was undertaken in order to study the temporal variation of wave fluxes in the MLT. Because we do not know the actual number of wave packets launched in any 2 h time interval, the following procedure was used. The momentum flux spectra for each interval were sampled as a function of horizontal wave number k_h , frequency ω , and azimuth ϕ for each point in the range $k_h \rightarrow k_h + dk_h$, $\omega \rightarrow \omega + d\omega$ and $\phi \rightarrow \phi + d\phi$. Here $dk_h = 2.53 \times 10^{-6} \text{ km}^{-1}$, $d\omega = 1.39 \times 10^{-4} \text{ s}^{-1}$ and $d\phi = 10^\circ$. Approximately 27,000 rays were launched, each with the appropriate model value of $u'w'(\omega, k_h, \phi)$. Such a large number of momentum flux samples mean that individual wave packets at the source level have very small amplitude, so that the majority of waves that do not encounter critical levels will propagate through the middle atmosphere without either saturating or breaking. Wave fluxes grow as $e^{z/H}$, where H is the density scale height, so that the total flux in the MLT would be very large if individual waves are launched with very small amplitudes.

[19] However, there are at least two factors that will produce much larger wave amplitudes at the source level than are derived from the Fourier analysis alone:

[20] 1. In Fourier space each spectral component $u'w'(\omega, k_h, \phi)d\phi dk_h d\omega$ has a scale proportional to $1/L$, where $L = 400 \text{ km}$. In real space, however, the wave fluxes as they emerge from the troposphere occupy only a fraction of the model domain, as illustrated in Figure 5.

[21] 2. The spectral values are the results of averaging over 2 h intervals. In practice, the temporal variability of the convective activity is on the time scale of minutes and has spatial variability on scales of the order of tens of km. This means that short-term peak wave fluxes will be much larger than the average values shown in Figure 5.

[22] There is no a priori way to determine the correction factor that should be applied to the initial fluxes in order to account for these factors. The method chosen was to use the actual flux measurements in the MLT to constrain their choice. The methodology adopted is described in section 4.2 after the details of the gravity wave ray tracing are discussed.

4. Gravity Wave Ray Tracing

4.1. Winds and Temperatures

[23] Middle atmosphere wind and temperature models are required to accurately trace the GW raypaths. To this end, a number of data sources were used to construct the zonal, $\bar{U}(z, t)$, meridional, $\bar{V}(z, t)$, and temperature, $\bar{T}(z, t)$, profiles as a function of height z and time t . First, daily mean profiles were obtained. Radiosonde soundings, which were made at 3 h intervals in the vicinity of Darwin during TWICE [May *et al.*, 2008], were averaged to construct the wind and temperature fields up to a height of 30 km. Zonal wind and temperature data obtained from the United Kingdom Meteorological Office (UKMO) assimilated data set, which were available for 12 UTC, were used between 30 and 65 km. For each height between 75 and 100 km hourly winds from the meteor radar were averaged to give the corresponding daily values for \bar{U} and \bar{V} . Since the meteor data are only available for 3 km height intervals these data were interpolated onto a 1 km height grid for the purposes of ray tracing. Data from the SABER instrument on the TIMED satellite were averaged for 00 and 12 UTC to give the diurnal mean \bar{T} between 75 and 100 km. Finally, the gap between the upper boundary from the UKMO data set and the 75 km lower boundary of the meteor data was interpolated over to get complete mean wind and temperature profiles.

[24] Time series of the zonal and meridional wind components at a mean height of 91 km are shown in Figure 6, with standard deviations of each hourly wind component derived using the technique described by Vincent *et al.* [2010]. Oscillations with tidal and 2 day wave periodicities are clearly apparent, with the 2 day wave having particularly large amplitudes at the start of the interval. Harmonic analysis

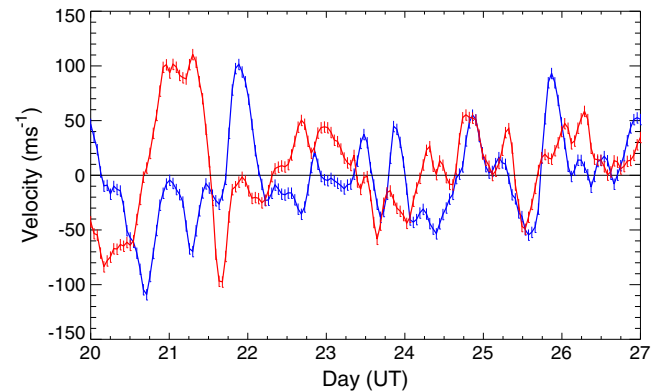


Figure 6. Time series of hourly average winds at 91 km measured using the meteor radar for the period 20–27 January 2006. The blue (red) curve is for the zonal (meridional) winds component. Vertical bars indicate the standard deviation of each component.

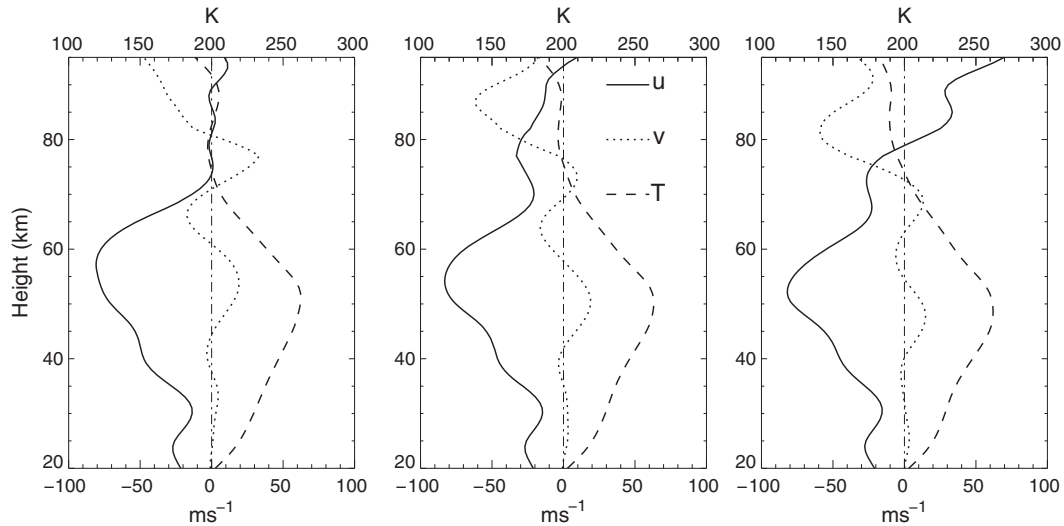


Figure 7. Vertical profiles of zonal (U), meridional (V), and temperature (T) over the height range 20–100 km for (left) 14 UTC, (center) 18 UTC, and (right) 22 UTC.

shows that over a 10 day interval centered on 23 January, the 2 day wave had mean amplitudes of 30 and 8 m s^{-1} in the NS and EW components, respectively, between 90 and 95 km. The corresponding values for the diurnal tide were about 30 m s^{-1} in both wind components with vertical wavelengths of ~ 25 km; for the semidiurnal tide, the amplitudes were about 10 m s^{-1} and it had a long vertical wavelength.

[25] While the meteor radar observations give the hourly MLT winds directly, the hourly temperature variations due to atmospheric tides need to be computed. Tidal temperatures were estimated from model calculations that were “calibrated” by the tidal winds derived from observations. Because of the large 2 day planetary-scale wave the meteor winds were harmonically analyzed in 2 day blocks using 48, 24, and 12 h components. Tidal wind parameters for the latitude and longitude around Darwin derived from the GSWM-02 model [Hagan and Forbes, 2002, 2003] compared well with the 24 and 12 h tidal parameters computed from the meteor winds; only small changes to the model amplitudes and phases were required to bring them into excellent agreement with observed values. After this calibration, the amplitude and phase of tidal temperature perturbations were then derived from GSWM-02 and superimposed on the diurnal mean temperature to provide hourly values at each height.

[26] Examples of vertical profiles of U , V , and T with 1 km and 1 h height and time resolutions are shown in Figure 7 for three times centered around the 23 January 2006 storm event. The mean zonal wind is dominated by the strong westward flow in the stratosphere, peaking near 55 km. This is typical of the phase of the tropical stratospheric semiannual oscillation at this time of the year. Strong tidal effects are also evident, especially above 80 km.

4.2. Ray-Tracing Results

[27] The gravity wave ray-tracing methodology used here follows the procedures described by Marks and Eckermann [1995]. Wave packets were launched from a height of 20 km and traced up to 100 km, with wave parameters stored after every step. In our calculations, the full

gravity wave dispersion relation was used to ensure that waves with high intrinsic frequencies were properly treated. The effects of wave dissipation were included, with a “climatological” eddy diffusion coefficient profile, D_{zz} , similar to that shown between 20 and 70 km in Figure 3 of Marks and Eckermann [1995] was used. Above 70 km, D_{zz} increased smoothly until above 80 km, it was held constant at a fixed value. In the initial ray-trace studies, this initial value was 400 $\text{m}^2 \text{s}^{-2}$.

[28] After each integration step, a number of checks were undertaken. One check was to ensure that the WKB approximations inherent in ray tracing were satisfied. If the assumptions were violated [equation (5) of Marks and Eckermann, 1995], the integration was terminated. Checks were also undertaken for wave instability and a saturation algorithm implemented if either dynamical or static instability was detected [see Marks and Eckermann, 1995 for further details].

4.3. Ray-Tracing Correction Factor

[29] As discussed in section 3, the flux corresponding to each packet $u'w'(\phi, k_h, \omega)$ was scaled before launch by a factor $\mathcal{F} \gg 1$ in order to correct for the temporal and spatial variability of the fluxes. After completion of each ray tracing, the flux was divided by \mathcal{F} to ensure that the total flux remained constant. This procedure is similar to the use of the intermittency factor in the Alexander and Dunkerton [1999] gravity wave parameterization scheme.

[30] To constrain \mathcal{F} requires, in principle, a knowledge of the momentum flux in the MLT, but it is not possible to measure momentum flux using a conventional all-sky meteor radar, at least on short time scales [Vincent et al., 2010]. However, Vincent et al. [2010] show that the kinetic energy per unit mass, $KE = (\overline{u'^2} + \overline{v'^2})$, can be measured with reasonable accuracy provided the meteor rates are high enough. The total KE was computed from the ray-tracing output as a function of height and time and compared with the measured values in order to find the optimum value of \mathcal{F} , as discussed below.

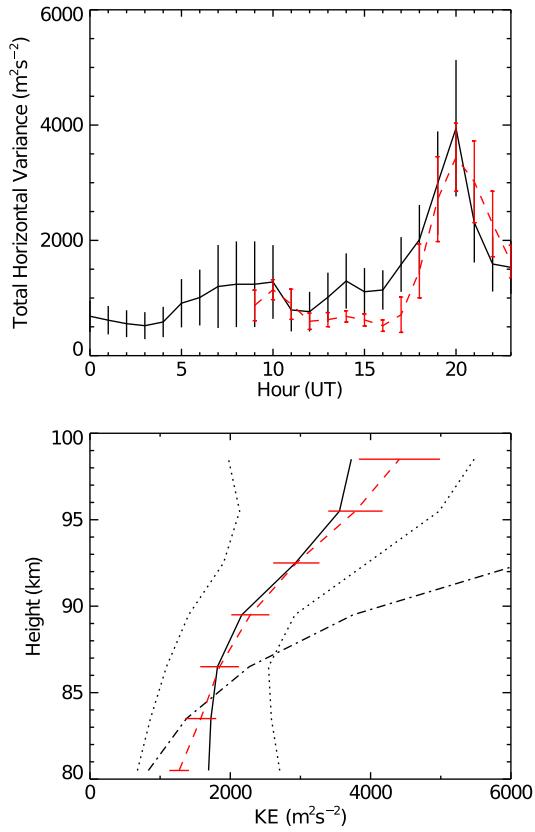


Figure 8. (top) Time series of gravity wave kinetic energy per unit mass ($KE = \overline{u'^2 + v'^2}$) derived from observations (solid) and ray tracing (red dashed) for a height of 92 km. The vertical bars indicate the uncertainty in KE derived from the meteor radar as discussed by Vincent *et al.* [2010], and the standard deviations in the model results. (bottom) The solid line shows the height profile of observed kinetic energy averaged over the time interval 19 to 21 UTC. The dotted lines give the upper and lower limits to the observed fluxes. The red dashed line and bars shows the mean computed energy flux and associated standard deviation (see text for details). The dash-dotted line shows how the energy would grow in the absence of dissipation or wave breaking.

[31] Further issues that needed consideration were (i) that the precise launch time of a packet within a 2 h time period was unknown and (ii) its horizontal position as the wavefield emerged into the lower stratosphere (c.f. Figure 5) was not known. To resolve these issues an iterative, stochastic approach was used.

[32] In the first step, the temporal and spatial issues were ignored and individual packets were launched from a height of 20 km at the center of a 2 h window and at the centroid of the flux pattern, such as that shown in Figure 5. After the ray tracing was complete for a given time interval, the total wavefield was reconstructed at each height by suitably combining the amplitudes of those waves that reached that height and the computed values compared with the observations. The process was repeated with a different \mathcal{F} until the total mean square wave amplitudes derived from the ray tracing approximately matched the observed KE values as a function of both time and height. If \mathcal{F} was too small, then

Table 1. Summary of Gravity Wave Propagation Times From 20 to 90 km Altitude and Radial Distances of the Ray Points at 90 km From Their Launch Position (R_o) and Meteor Radar (R_m)^a

Quantity	Median	Mean
Time (h)	1.03	1.23
R_o (km)	190	244
R_m (km)	220	265

^aThe results pertain to a 2 h period centered on 20 UTC.

insufficient wave breaking occurred in the middle atmosphere and wave amplitudes in the MLT were too large compared with observations. Conversely, if \mathcal{F} was too large then the waves saturated or broke too low in the middle atmosphere and the resultant wave amplitudes in the MLT were too small compared with the measurements.

[33] The best match between computed and observed variances was when $\mathcal{F} \sim 500$. To put this figure in context, at the launch height the median value of $u'w'(\phi, k_h, \omega)d\phi dk_h d\omega$ was $\sim 7 \times 10^{-7}$ Pa. When scaled by \mathcal{F} , this meant the packet value was $\sim 3.5 \times 10^{-4}$ Pa. It is also noted that if \mathcal{F} is varied by $\pm 20\%$, i.e., between values of ~ 400 and 600 , then the agreement between the computed and measured KE time and height profiles is not as good, but still within the error bounds.

[34] Once the best value of \mathcal{F} was found then the second step was to repeat the process many times with this value of \mathcal{F} , but each time randomly choosing the time of launch of each ray (within a the 2 h window) and its horizontal position. This process gave a large number of time series and height profiles of wave fluxes, which when averaged, provided a measure of the statistical variation in the ray-traced fluxes. It should be noted that any rays that propagated sufficiently far horizontally to pass outside the meteor radar

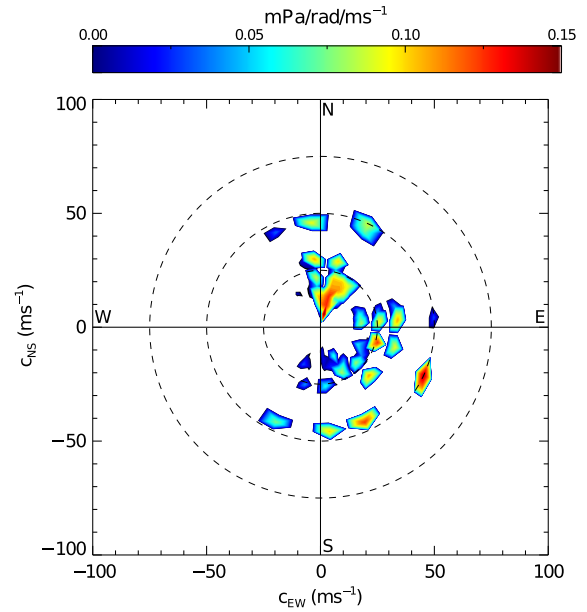


Figure 9. The mean angular spectrum of gravity wave absolute momentum flux at 90 km derived from ray-tracing studies as a function of ground-based phase speed. The results are for 20 UTC. The dashed circles denote speeds of 25, 50, and 75 m s⁻¹.

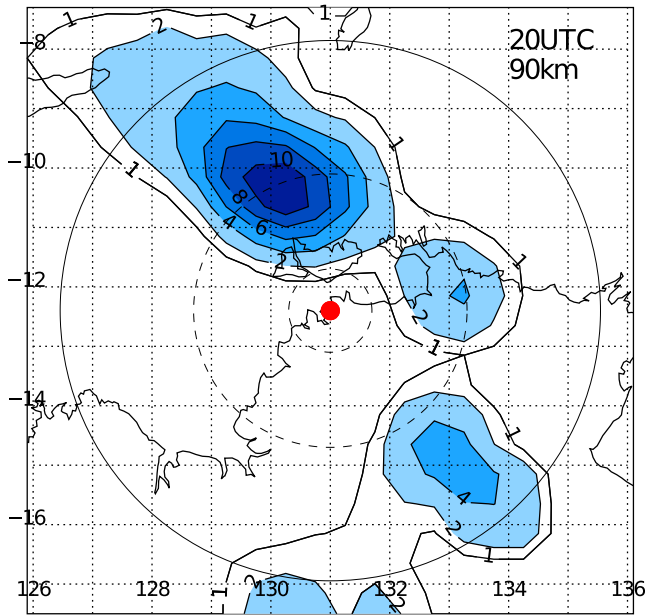


Figure 10. Geographic variation of momentum flux per unit mass ($\sqrt{|u'w'|^2 + |v'w'|^2}$) computed from GW ray-tracing results for a height of 90 km at 20 UTC. The peak value is about $13 \text{ m}^2 \text{ s}^{-2}$. The red dot shows the position of the meteor radar and the circles show the radar coverage at 40° , 60° , and 80° from the zenith.

observing region were not used when it came to computing the variances. However, all results were retained in order to compute momentum fluxes.

[35] The overall result is shown in Figure 8, where the observed GW variances and their uncertainties are compared with the computed fluxes and their uncertainties. There is good agreement, especially when it is noted that the observed values have quite large uncertainty. Not unexpectedly, both observed and computed fluxes grow more slowly with altitude than the $\exp(z/H)$ factor which would be expected if wave breaking and dissipation were not taking place.

[36] Before considering the momentum flux variations other results from the ray-tracing analysis are discussed. Table 1 summarizes parameters derived from the GW ray-tracing output derived from the optimized value of \mathcal{F} discussed above. The results pertain to the 2 h interval centered on 20 UTC, but are representative of other times. The majority of the waves that reach the MLT do so within about 2 h of launch and within a radial distance of about 220 km from the center of the meteor radar observing region, which is optimum for the meteor radar wind determinations. The mean lateral displacement of rays reaching the MLT from their launch position at 20 km altitude is about 200–240 km.

[37] Figure 9 shows the angular spectrum of momentum flux at a mean height of 90 km. The plot is an average computed from all the ray-tracing results and was constructed for all wave packets arriving within the 2 h interval centered on 20 UTC. Comparing this spectrum with the launch spectrum (Figure 3), it is apparent that essentially most waves propagating westward have been removed, as have many eastward propagating waves with phase speeds less than 25 m s^{-1} .

[38] Two factors are involved. First, there is wave filtering by the background wind and temperatures. Waves are removed at critical levels where the ground-based phase speed of a wave is equal to the background wind speed. Inspection of Figure 7 suggests critical level filtering particularly affected waves propagating westward in the stratosphere and southward at heights above about 75 km. Furthermore, waves launched with particularly large amplitudes at 20 km will saturate when

$$(u'^2 + v'^2)^{1/2} = U' \sim |\bar{U} - c|, \quad (1)$$

where \bar{U} is the mean wind in the direction of phase propagation and c is the ground-based phase speed. In this situation, U' remains constant with height until, or if, (1) is no longer satisfied when such waves will start to grow again. Figures 3 and 7 suggest that the condition specified by (1) is most likely to occur for slower, eastward propagating waves that encounter regions of low zonal wind speed in the mesosphere. The net effect is to reduce eastward propagating wave fluxes in the MLT. Finally, it is noticeable in Figure 9 that there is a tendency for waves propagating toward the SE to have discrete phase speeds with values near 25 and 50 m s^{-1} . These may be associated with the peaks evident in the source spectrum in Figure 4.

[39] Our results are in accord with others, such as Preusse et al. [2008], which show that the shortest waves are removed by wind shear and slower waves by

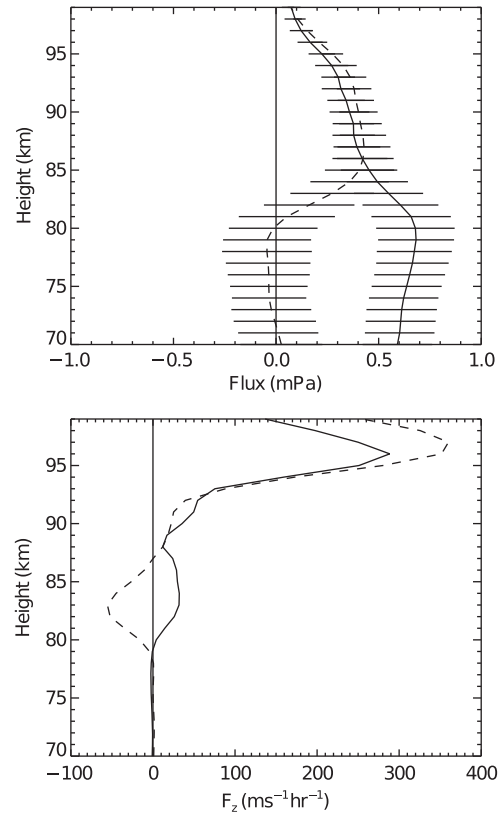


Figure 11. (top) Vertical profiles of zonal (solid) and meridional (dashed) momentum flux in units of mPa for 20 UTC. The bars indicate the standard deviation. (bottom) Vertical profiles of the body force per unit mass ($\text{m s}^{-1} \text{ h}^{-1}$).

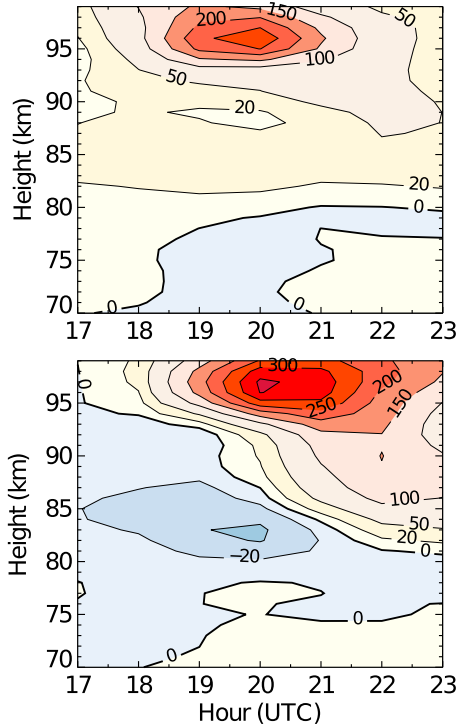


Figure 12. Time-height cross section of (top) zonal and (bottom) meridional body force per unit mass. Red/yellow colors indicate eastward (northward) components while blue colors indicate westward (southward) components. Units are $\text{m s}^{-1} \text{h}^{-1}$.

critical level interactions. The highest phase speed waves attain large vertical wavelengths and travel rapidly to the MLT, with the capacity to transport large amounts of momentum.

[40] As well as filtering out westward and southward propagating waves, the background winds also advect wave packets, affecting their geographic location as they reach the MLT. Despite the eastward bias in the source spectra (Figure 3) the strong westward winds in the stratosphere mean that the majority of packets reach the MLT to the north-west of Darwin, as illustrated in Figure 10. Most of the flux (55%) is located to the NW of the radar, but there are patches of significant flux to the east, south-east, and south.

5. Momentum Fluxes

[41] Once the wave fluxes had been calibrated and their uncertainties derived, it was then possible to compute the mean momentum flux as a function of height and time, as illustrated in Figure 11 for 20 UTC in the MLT. The top panel shows height variations of $\rho_o \overline{u'w'}$ and $\rho_o \overline{v'w'}$. It should be noted that $u'w'$ and $v'w'$ were computed for the whole of the geographic region shown in Figure 10. For the meridional flux, there is a change in sign from small negative (southward) fluxes below 80 km to positive fluxes above, with a steady reduction in magnitude above 85 km. The zonal fluxes are positive (eastward) at all heights and steadily decrease in magnitude above 80 km.

[42] The vertical gradients in the momentum fluxes means that there are associated body forces given by

$$F_z(x, y) = \left(-\frac{1}{\rho_o} \frac{\partial(\rho_o \overline{u'w'})}{\partial z}, -\frac{1}{\rho_o} \frac{\partial(\rho_o \overline{v'w'})}{\partial z} \right). \quad (2)$$

The computed F_z for 20 UTC is shown in the bottom panel of Figure 11. The main feature is a region of large eastward and northward body forces of magnitude $\sim 300 \text{ m s}^{-1} \text{h}^{-1}$. Below 90 km, there are secondary regions centered near 85 km showing enhanced eastward and southward directed forces.

[43] A time-height contour plot of F_z (Figure 12) shows that the region of strong eastward acceleration at 95–100 km occurs primarily between 18 and 22 UTC and that there is a region of small westward F_z below 80 km. The meridional forces have more of a dipole character. There are strong northward values in the upper MLT and southward values below, with a pronounced southward peak between 19 and 20 UT located near 85 km. The region between the northward and southward F_z descends with time at about 1–2 km/h. This seems to parallel the descent of the NS tidal wind field evident in Figure 7.

6. Summary and Discussion

[44] On 23 January 2006, during the TWIPCE campaign centered on Darwin, Australia, a strong, relatively isolated mesoscale convective system (MCS) occurred in the lower atmosphere. Nearly simultaneously, large gravity wave energy fluxes with peak amplitudes of about $4000 \text{ m}^{-2} \text{s}^{-2}$ were inferred from meteor radar wind observations at heights near 90 km in the upper mesosphere/lower thermosphere. In this study, a combination of techniques were used to investigate gravity wave generation by the MCS and their propagation and dissipation in the middle atmosphere and their association with the waves observed in the MLT. In summary

[45] 1. CPol, a scanning polarimetric weather radar, was used to determine maps of hydrometeor distributions within a radius of 150 km and up to heights near 20 km.

[46] 2. The three-dimensional CPol rain rates were then used to derive latent heating rates in a high-resolution non-hydrostatic numerical model that, in turn, computed gravity wave fluxes at heights near 20 km. The momentum flux spectrum was computed in 2 h blocks, each overlapped by 1 h, in order to capture as wide a part of the gravity wave spectrum as possible, but with reasonable time resolution.

[47] 3. The model flux output was used in conjunction with numerical gravity wave ray-tracing techniques to derive the wave spectrum in the MLT up to heights near 100 km. Computed energy fluxes were compared as a function of height and time with the fluxes measured by the meteor wind radar.

[48] 4. To achieve realistic comparisons it was necessary to scale the model wave fluxes using an iterative, stochastic, approach to find an appropriate scaling factor and model the effects of temporal and spatial variability of the waves launched from 20 km.

[49] 5. The majority of the waves that reached heights near 90 km did so within 1–2 h of launch and propagated laterally only about 200–250 km from the center of the storm.

[50] 6. Momentum fluxes deduced from the calibrated ray-tracing studies show strong flux convergence in the 80–100 km height region. Eastward and northward directed body forces of up to several hundred $\text{m s}^{-1} \text{h}^{-1}$ with durations of 3–4 h were inferred in the 95–100 km region. The region of strong wave breaking descended with time.

6.1. Uncertainties

[51] This study shows the benefit of using a number of complementary techniques to study gravity wave generation, propagation and momentum flux deposition in the upper middle atmosphere. A relatively simple gravity wave ray-tracing methodology was used, in that the spatial and temporal variability of the wind and temperature fields were ignored and an ad hoc eddy damping profile used. This allowed the modeling of the dynamical interactions in the MLT without too many complications. However, some of the simplifications need to be justified and their possible impact on the results assessed.

[52] *Eckermann and Marks* [1996] explored how tide-gravity wave interactions can affect the ray-tracing results. However, we do not believe that these effects are significant in this study because of the high intrinsic frequency of the waves and their short transit times from the region of generation to the MLT, (see Table 1). As far as the majority of the waves are concerned, the tidal winds vary sufficiently slowly that they look like “prevailing winds.”

[53] Spatial variations in the tidal wind and temperature fields may also affect the results. The MLT winds used in the model are derived using the all-sky meteor wind technique, which assumes that the mean wind field is constant across the whole field of view of the radar. This assumption may not hold in the NS direction at tropical latitudes where the diurnal tidal amplitudes increase poleward [*Hagan and Forbes*, 2002]. Results from the GSWM09 model (M. Hagan, private communication, 2012) and from observational studies [e.g., *Manson et al.*, 2002] show, however, that the latitudinal gradient in tidal amplitudes is only of the order of a few meters per second in the 9°S–15°S latitudinal range, and therefore, such spatial gradients are not likely to impact significantly on our basic results.

[54] Strong wave breaking evident in the MLT after 18 UTC is likely to lead to more turbulence thereby increasing the eddy diffusivity and therefore stronger wave dissipation. Sensitivity studies were also used to investigate the potential impacts of changing the eddy dissipation profile. However, it was found that increasing D_{zz} from the nominal value of 400 to 800 $\text{m}^2 \text{s}^{-2}$ did not have major impact on the results. The most important factors affecting the spectrum of waves in the MLT were the effects of wind filtering and wave reflection in the middle atmosphere.

[55] Aside from the uncertainties in GW ray tracing imposed by incomplete knowledge of the background state of the atmosphere, there are other uncertainties due to incomplete knowledge of the physical processes involved in wave generation. In particular, the wave fluxes emerging from the troposphere were based on numerical modeling that assumed a half-cosine vertical profile of latent heat release. In practice, the heating process may have been more complex because rainfall measurements made with the VHF boundary layer radar found that evaporation occurred

at heights below 1 km. The corresponding cooling of the lowest part of the atmosphere would result in an increase in the peak heating rate, assuming that the total heating remained the same [e.g., *Grimsdell et al.*, 2010, their Figure 11]. Increases in peak heating rates of 75% or more may be inferred if the evaporation process extended over the whole part of the storm. This would lead to a corresponding change in the fluxes emerging from the troposphere. Since we used the meteor radar observations to “calibrate” wave fluxes any changes in the magnitude of the momentum fluxes leaving the troposphere would not materially affect the results. This would not be the case if changing the heating profile significantly changed the momentum flux spectrum as a function of phase speed and frequency, for example.

[56] There is also an inherent selection process imposed by the choice of the domain size of the numerical model. Waves with horizontal wavelengths significantly smaller than the domain will be better resolved than waves that have scales similar to the domain.

[57] In summary, the limitations of our analysis imposed by incomplete knowledge of the physical processes in the source spectrum and the intervening atmosphere through which the waves propagate do not change our overall conclusions. That is, gravity wave momentum deposition led to strong accelerations in the MLT, localized in both time and space.

6.2. Spatial Variability

[58] To place our results in context, we note that the convective event on 23 January was one of four convective storms that occurred during the 25 day duration TWICE campaign. It was, however, the largest such event. With a duration of less than 5 h it would be classified as a “short” MCS by *Pope et al.* [2009], who made an extensive analysis of the occurrence of MCSs in and around northern Australian. Between November and April for the 6 year period between 1995 and 2001, they found 13,585 MCSs occurred in the region extending from 5°S to 25°S in latitude and 120°E to 150°E in longitude. In broad terms, this means about 12 MCS per day in the whole region, although there was seasonal and geographical variability in the four classes of MCS that *Pope et al.* [2009] considered.

[59] Our results support the conclusions of *Vadas and Fritts* [2002] who emphasized that the zonal mean body force required to close the mesospheric jets is sporadic and localized in space and time. Hence, global models that have coarse resolution may miss a significant source of sporadic wave drag. If our results are representative of all MCS events, then these statistics provide some insight into how to include GW effects in numerical models. For example, the Whole Atmosphere Community Climate Model in its Thermospheric extension (WACCM-X) uses a $1.9^\circ \times 2.5^\circ$ latitude/longitude grid box [*Liu et al.*, 2010], which means that an MCS event can be expected to occur approximately once every 10 days in each model grid box during the November to April northern Australian wet season. As an aside, it is noted that the typical lateral dispersion of about 220 km or about 2° (Table 1) suggests that the GW effects in the MLT would be felt in grid boxes adjacent to the box from which the waves were launched.

6.3. The Transient Response

[60] Understanding how the atmosphere responds to the transient forcing in space and time evident in our results is outside the scope of this paper, but some consequences can be discussed qualitatively. One consequence is the generation of secondary waves by the overall wave breaking processes.

[61] First, it is noted that one response to transient momentum deposition is the excitation of waves with near tidal periods [Walterscheid, 1997]. Large day-to-day variability of the MLT wind field on tidal time scales is a well-known phenomenon and is clearly evident in Figure 6. Averaging over several days is required to extract meaningful tidal parameters from MLT radar observations. Tidal transience can be caused both by the localized nature of the tropospheric latent heat release and by the localized nature of the body forces associated with the momentum flux deposition in the MLT, as observed here.

[62] Second, the transient response will be manifested in the generation of secondary gravity waves in the upper atmosphere [Zhou et al., 2002; Vadas and Fritts, 2002; Vadas et al., 2003; Chun and Kim, 2008; Vadas and Liu, 2009]. The efficiency of secondary wave generation depends on the time scale of the forcing event relative to a characteristic time scale that depends in turn on the spatial extent of the body forces.

[63] It is outside the scope of this paper to make a complete analysis of the atmospheric response to the body forcing, but some preliminary estimates can be made using a simplified analytic approach. Figure 10 shows that in the horizontal, the forcing occurs in patches that are approximately elliptical in shape with Gaussian cross sections. The largest patch is centered on (130°E, 10.5°S). In the vertical, the forcing may also be described as approximately Gaussian, centered on a mean height near 98 km (Figure 11), so the spatial distribution of the body force may be described as an ellipsoidal “pancake.” Following a similar notation to Vadas et al. [2003], the force is approximated as

$$F(\mathbf{x}) = F_o \exp \left[-\frac{1}{2} \left(\frac{(x-x_o)^2}{\sigma_x^2} + \frac{(y-y_o)^2}{\sigma_y^2} + \frac{(z-z_o)^2}{\sigma_z^2} \right) \right]. \quad (3)$$

where $\mathbf{x} = (x, y, z)$ and the (x, y) axes are aligned along the major (NW-SE) and minor (NE-SW) axes of the ellipsoid. The centroid is located at $(x_o, y_o) = (130.2^\circ\text{E}, 10.5^\circ\text{S})$ and altitude $z_o = 98$ km. To first order, the spatial parameters are estimated to be $\sigma_x \sim 120$ km, $\sigma_y \sim 80$ km, and $\sigma_z \sim 3.5$ km.

[64] From the dispersion equation for gravity waves at low latitudes, where the inertial frequency f is small, the wave frequency is

$$\omega = \left(\frac{N^2 k_h^2}{k_h^2 + m^2 + 1/4H^2} \right)^{1/2}, \quad (4)$$

where the wave number $\mathbf{k} = (k, l, m)$ and $k_h^2 = k^2 + l^2$. Following Vadas et al. [2003], a characteristic source intrinsic frequency ω_c can be derived from the characteristic scales ($\sigma_x = 1/k$, $\sigma_y = 1/l$, $\sigma_z = 1/m$) to give

$$\omega_c = \left(\frac{(\sigma_x^{-2} + \sigma_y^{-2})N^2}{\sigma_x^{-2} + \sigma_y^{-2} + \sigma_z^{-2} + 1/4H^2} \right)^{1/2} = \left(\frac{\sigma_h^{-2}N^2}{\sigma_h^{-2} + \sigma_z^{-2} + 1/4H^2} \right)^{1/2}. \quad (5)$$

With the above values for the characteristic spatial scales, the characteristic period is estimated to be $\tau_c = 2\pi/\omega_c \sim 100$ min.

[65] This value is similar to the temporal scale of the forcing event (Figure 12), so secondary GW wave forcing could be reasonably efficient. For those waves that are forced, the relatively shallow nature of the forcing region, which has an aspect ratio (vertical to horizontal) of $L_z/L_h = \sigma_z/\sigma_h = 3.5/66 = 0.05$, means that low-frequency secondary waves are most likely to be emitted [Vadas et al., 2003]. Nevertheless, the quite large overall depth of the forcing region (~ 10 km) implies that some waves with quite high intrinsic frequencies will be generated.

[66] An interesting and complicating factor caused by any generation of secondary waves is that our analysis and calibration of wave fluxes depend on the assumption that the KE variances centered on 20 UTC (Figure 8) are due solely to the primary GWs that propagate directly from the troposphere. The presence of any secondary waves with ground-based periods less than 2 h both broadens and increases the amplitude of the KE peak, thereby affecting the calibration of the ray-tracing wave amplitudes. Since we cannot distinguish primary from secondary waves in the meteor wind analysis, it is not possible to quantify what influence secondary waves have, although it means that the factor \mathcal{F} , which sets the ray-tracing wave amplitudes, is likely to be overestimated.

[67] Secondary wave effects are not just limited to the MLT but will be felt both down in the middle atmosphere and higher up in the thermosphere [e.g., Vadas et al., 2003; Chun and Kim, 2008]. Downward propagating waves have implications for the middle atmosphere momentum budget and parameterization schemes, which currently do not include such waves, and their ability to redistribute momentum. Similarly, the transfer of wave influences into the upper atmosphere will induce thermospheric body forces and ionospheric disturbances.

[68] There are other aeronomic influences as well. At short periods, secondary wave generation at altitudes near 95 km may account for the characteristics of small-scale ($\lambda_h \sim 10$ –80 km) short period (10–50 min) GWs observed in airglow at these heights. Hecht et al. [1997] reported a strong seasonal variation in the directionality of GW-induced variations in OH and O₂ band emission lines. Quasi-monochromatic features were observed at Adelaide (35°S, 138°E) to propagate primarily southward in summer. Walterscheid et al. [1999] interpreted this anisotropy in terms of waves propagating in thermal ducts located near the mesopause from distant sources to the north of Adelaide. They suggested that convectively generated waves from tropical northern Australia during the wet season might be the cause of the anisotropy. Further studies by Walterscheid et al. [2001] and Walterscheid and Hickey [2009] found that direct injection of waves energy into the ducts from tropospheric convective sources was possible. However, we suggest that the injection of secondary GWs generated at or near the duct level in the MLT may be a more efficient process for getting wave energy into a duct.

[69] In conclusion, a variety of experimental and computational techniques were used to explore the upper atmosphere response to gravity waves launched from an MCS in the tropical lower atmosphere in the vicinity of Darwin,

Australia. The impact of momentum deposition in the MLT was manifested as a large transient north-eastward directed body force. The direction and magnitude of the forcing were primarily due to three factors. The first is the spectral composition of the waves generated by the temporal and spatial distribution of the latent heat release in the troposphere. The second factor was the wave filtering due to the wind distribution in the middle atmosphere, and third was the filtering due to the tidal winds in the MLT itself. Other factors, such as eddy dissipation, were less important in the height and strength of the momentum deposition. The importance of the tidal wind structure in determining the final direction of the body force is apparent when subsidiary calculations were made in which all parameters were retained except that the ray tracing was carried at a notional time 12 h earlier, when the tidal wind fields were reversed. The momentum flux deposition and body force were now directed toward the south-east but had about the same magnitude. Overall, the results point to the importance of short period, short wavelength gravity waves for the momentum budget of the MLT.

[70] **Acknowledgments.** We thank R. Garcia for provision of the TIMED/SABER data and M. Hagan for the use of the GSWM tidal model. UKMO wind and temperature data were provided by the British Atmospheric Data Centre. The helpful comments by R. L. Walterscheid on an earlier draft of the MSS are appreciated. This work was supported by Australian Research Council grant DP0558361. MJA was supported by Physical and Dynamic Meteorology at the National Science Foundation, award 0943506.

References

- Alexander, M. J., and T. J. Dunkerton (1999), A spectral parameterization of mean-flow forcing due to breaking gravity waves, *J. Atmos. Sci.*, **56**, 4167–4182.
- Alexander, M. J., and J. R. Holton (2004), On the spectrum of vertically propagating gravity waves generated by a transient heat source, *Atmos. Chem. Phys.*, **4**, 923–932.
- Alexander, M. J., P. T. May, and J. H. Beres (2004), Gravity waves generated by convection in the Darwin area during the Darwin Area Wave Experiment, *J. Geophys. Res.*, **109**, D20S04, doi:10.1029/2004JD004729.
- Beres, J. H., M. J. Alexander, and J. R. Holton (2004), A method of specifying the gravity wave spectrum above convection based on latent heating properties and background wind, *J. Atmos. Sci.*, **61**, 324–337.
- Beres, J. H., R. R. Garcia, B. A. Boville, and F. Sassi (2005), Implementation of a gravity wave source spectrum parameterization dependent on the properties of convection in the Whole Atmosphere Community Climate Model (WACCM), *J. Geophys. Res.*, **110**, D10108, doi:10.1029/2004JD005504.
- Bringi, V. N., M. Thurai, K. Nakagawa, G. J. Huang, T. Kobayashi, A. Adachi, H. Hanado, and S. Sekizawa (2006), Rainfall estimation from C-band polarimetric radar in Okinawa, Japan: Comparisons with 2D-video disdrometer and 400 MHz wind profiler, *J. Meteor. Soc. Japan*, **84**, 705–724.
- Bringi, V. N., C. R. Williams, M. Thurai, and P. T. May (2009), Using dual-polarized radar and dual-frequency profiler for DSD characterization: A case study from Darwin, Australia, *J. Atmos. and Oceanic Technol.*, **26**, 2107–2122.
- Chun, H.-Y., and Y.-H. Kim (2008), Secondary waves generated by breaking of convective gravity waves in the mesosphere and their influence in the wave momentum flux, *J. Geophys. Res.*, **113**, D23107, doi:10.1029/2008JD009792.
- Eckermann, S. D., and C. J. Marks (1996), An idealized ray model of gravity wave-tidal interactions, *J. Geophys. Res.*, **101**, 21195–21212.
- Fritts, D. C., and M. J. Alexander (2003), Gravity wave dynamics and effects in the middle atmosphere, *Rev. Geophys.*, **41**, 1003, doi:10.1029/2001RG000106.
- Grimsdell, A. W., M. J. Alexander, P. T. May, and L. Hoffmann (2010), Model study of waves generated by convection with direct validation via satellite, *J. Atmos. Sci.*, **67**, 1617–1631.
- Hagan, M. E., and J. M. Forbes (2002), Migrating and nonmigrating diurnal tides in the middle and upper atmosphere excited by tropospheric latent heat release, *J. Geophys. Res.*, **107**, 4754, doi:10.1029/2001JD001236.
- Hagan, M. E., and J. M. Forbes (2003), Migrating and nonmigrating semidiurnal tides in the upper atmosphere excited by tropospheric latent heat release, *J. Geophys. Res.*, **108**, 1062, doi:10.1029/2002JA009466.
- Hamilton, K., R. A. Vincent, and P. T. May (2004), Darwin Area Wave Experiment (DAWEX) field campaign to study gravity wave generation and propagation, *J. Geophys. Res.*, **109**, D20S01, doi:10.1029/2003JD004393.
- Hecht, J. H., R. L. Walterscheid, J. Woihe, L. Campbell, R. A. Vincent, and I. M. Reid (1997), Trends in airglow imager observations near Adelaide, Australia, *Geophys. Res. Lett.*, **24**, 587–590.
- Hecht, J. H., S. Kovalam, P. T. May, G. Mills, R. A. Vincent, R. L. Walterscheid, and J. Woihe (2004), Airglow imager observations of atmospheric gravity waves at Alice Springs and Adelaide, Australia, during the Darwin Area Wave Experiment (DAWEX), *J. Geophys. Res.*, **109**, D20S05, doi:10.1029/2004JD004697.
- Hines, C. O. (1997), Doppler-spread parameterization of gravity-wave momentum deposition in the middle atmosphere. Part 1: Basic formulation, *J. Atmos. Solar-Terr. Phys.*, **59**, 371–386.
- Holdsworth, D. A., I. M. Reid, and M. A. Cervera (2004), Buckland Park all-sky interferometric meteor radar, *Radio Sci.*, **39**, RS5009, doi:10.1029/2003RS003014.
- Holton, J. R., and M. J. Alexander (1999), Gravity waves in the mesosphere generated by tropospheric convection, *Tellus*, **51**(A–B), 45–58.
- Horinouchi, T. (2004), Simulated breaking of convectively generated mesoscale gravity waves and airglow modulation, *J. Atmos. Solar-Terr. Phys.*, **66**, 755–767.
- Horinouchi, T., T. Nakamura, and J.-I. Kosaka (2002), Convectively generated meso-scale gravity waves simulated throughout the middle atmosphere, *Geophys. Res. Lett.*, **29**(2007), doi:10.1029/2002GL016069.
- Kim, S. Y., H.-Y. Chun, and J.-J. Baik (2007), Sensitivity of typhoon-induced gravity waves to cumulus parameterizations, *Geophys. Res. Lett.*, **34**, L15814, doi:10.1029/2007GL030592.
- Lane, T. P., M. J. Reeder, and F. M. Guest (2003), Convectively generated gravity waves observed from radiosonde data taken during MCTEX, *Quart. J. Roy. Meteor. Soc.*, **129**, 1731–1740.
- Lane, T. P., and R. D. Sharman (2006), Gravity wave breaking, secondary wave generation, and mixing above deep convection in a three-dimensional cloud model, *Geophys. Res. Lett.*, **33**, L23813, doi:10.1029/2006GL027988.
- Lane, T. P., and M. W. Moncrieff (2008), Stratospheric gravity waves generated by multiscale tropical convection, *J. Atmos. Sci.*, **65**, 2598–2614.
- Lindzen, R. S. (1981), Turbulence and stress owing to gravity wave and tidal breakdown, *J. Geophys. Res.*, **86**, 9707–9714.
- Liu, H. L., et al. (2010), Thermosphere extension of the whole atmosphere community climate model, *J. Geophys. Res.*, **115**, A12302, doi:10.1029/2010JA015586.
- Marks, C. J., and S. D. Eckermann (1995), A Three-dimensional nonhydrostatic ray-tracing model for gravity waves: Formulation and preliminary results for the middle atmosphere, *J. Atmos. Sci.*, **52**, 1959–1984.
- Manson, A. H., Y. Luo, and C. Meek (2002), Global distributions of diurnal and semi-diurnal tides: Observations from HRDI-UARS of the MLT region, *Annals Geophys.*, **20**, 1877–1890.
- May, P. T., J. H. Mather, G. Vaughan, C. Jakob, G. M. McFarquhar, K. N. Bower, and G. G. Mace (2008), The tropical warm pool international cloud experiment, *Bull. Amer. Meteor. Soc.*, **89**, 629–644.
- Palmer, T. N., G. J. Shutts, and R. Swinbank (1986), Alleviation of a systematic westerly bias in general circulation and numerical weather prediction models through orographic gravity wave parameterization, *Quart. J. Roy. Meteor. Soc.*, **112**, 1001–1039.
- Piani, C., D. Durran, M. J. Alexander, and J. R. Holton (2000), A numerical study of three-dimensional gravity waves triggered by deep tropical convection and their role in the dynamics of the QBO, *J. Atmos. Sci.*, **57**, 3689–3702.
- Pope, M., C. Jakob, and M. J. Reeder (2009), Objective classification of tropical mesoscale convective systems, *J. Climate*, **22**, 5797–5808.
- Preusse, P., S. D. Eckermann, and M. Ern (2008), Transparency of the atmosphere to short horizontal wavelength gravity waves, *J. Geophys. Res.*, **113**, D24104, doi:10.1029/2007JD009682.
- Song, I.-S., H.-Y. Chun, and T. P. Lane (2003), Generation mechanisms of convectively forced internal gravity waves and their propagation to the stratosphere, *J. Atmos. Sci.*, **60**, 1960–1980.
- Song, I.-S., H.-Y. Chun, R. R. Garcia, and B. A. Boville (2007), Momentum flux spectrum of convectively forced internal gravity waves and its application to gravity wave drag parameterization. Part II: Impacts in a GCM (WACCM), *J. Atmos. Sci.*, **64**, 2286–2308.

- Vadas, S. L., and D. C. Fritts (2002), The importance of spatial variability in the generation of secondary gravity waves from local body forces, *Geophys. Res. Lett.*, **29**, 1984, doi:10.1029/2002GL015574.
- Vadas, S. L., D. C. Fritts, and M. J. Alexander (2003), Mechanism for the generation of secondary waves in wave breaking regions, *J. Atmos. Sci.*, **60**, 194–214.
- Vadas, S. L., and H.-L. Liu (2009), Generation of large-scale gravity waves and neutral winds in the thermosphere from the dissipation of convectively generated gravity waves, *J. Geophys. Res.*, **114**, A10310, doi:10.1029/2009JA014108.
- Vadas, S. L., and G. Crowley (2010), Sources of the traveling ionospheric disturbances observed by the ionospheric TIDDBIT sounder near Wallops Island on 30 October 2007, *J. Geophys. Res.*, **115**, A07324, doi:10.1029/2009JA015053.
- VanZandt, T. E. (1985), A model for gravity wave spectra observed by Doppler sounding systems, *Radio Sci.*, **20**, 1323–1330.
- Vincent, R. A., A. D. MacKinnon, I. M. Reid, and M. J. Alexander (2004), VHF profiler observations of winds and waves in the troposphere during the Darwin Area Wave Experiment (DAWEX), *J. Geophys. Res.*, **109**, D20S02, doi:10.1029/2004JD004714.
- Vincent, R. A., S. Kovalam, I. M. Reid, and J. P. Younger (2010), Gravity wave flux retrievals using meteor radars, *Geophys. Res. Lett.*, **37**, L14802, doi:10.1029/2010GL044086.
- Walterscheid, R. L. (1997), Simple models of tidal transience: The steady signal, *J. Geophys. Res.*, **102**, 25,807–25,815.
- Walterscheid, R. L., G. Schubert, and D. G. Brinkman (2001), Small-scale gravity waves in the upper troposphere and lower thermosphere generated by deep tropical convection, *J. Geophys. Res.*, **106**, 31,825–31,832.
- Walterscheid, R. L., J. H. Hecht, R. A. Vincent, I. M. Reid, J. Woithe, and M. P. Hickey (1999), Analysis and interpretation of airglow and radar observations of quasi-monochromatic gravity waves in the upper mesosphere and lower thermosphere over Adelaide, Australia (35S, 138E), *J. Atmos. Solar-Terr. Phys.*, **61**, 461–478.
- Walterscheid, R. L., and M. P. Hickey (2009), Gravity wave ducting in the upper mesosphere and lower thermosphere duct system, *J. Geophys. Res.*, **114**, D19109, doi:10.1029/2008JD011269.
- Warner, C. D., and M. E. McIntyre (2001), An ultrasimple spectral parameterization for nonorographic gravity waves, *J. Atmos. Sci.*, **58**, 1837–1857.
- Webster, P. J., and R. Lukas (1992), TOGA COARE: The coupled ocean-atmosphere response experiment, *Bull. Amer. Meteor. Soc.*, **73**, 1377–1416.
- Zhou, X.-L., J. R. Holton, and G. L. Mullendore (2002), Forcing of secondary waves by breaking of gravity waves in the mesosphere, *J. Geophys. Res.*, **107**, 4058, doi:10.1029/2001JD001204.